nature portfolio

https://doi.org/10.1038/s41550-021-01532-8

## Supplementary information

# Probable detection of an eruptive filament from a superflare on a solar-type star

In the format provided by the authors and unedited

# Supplementary Information

**Basic relation between solar filament eruptions and CMEs** In the case of solar flares, eruptive phenomena can be often observed as low-lying cool-mass eruptive phenomena (known as filament or prominence eruptions via H$\alpha$; cf. section "Solar data analysis") and CMEs (e.g., via coronagraph). The CMEs often consist of faster, upper regions (known as "leading edges") and slower, lower regions (known as "cores"). It is thought that the CME cores and leading edges consist of the dense material of filament eruptions and the outer hot-coronal mass, respectively[90].

The typical velocities of solar CMEs are 20–3,000 km s$^{-1}$ (ref.[90], Fig. 14 of ref.[2]). On the other hand, those of filament eruptions accompanied by CMEs are 10–400 km s$^{-1}$ (Fig. 14-15 of ref.[2]). Consequently, the filament eruptions velocities are minor because the filament eruptions correspond to the lower region of the self-similarly expanding CMEs. Because of this, there are solar eruptive events with a large amount of lower cool-filament masses that has fallen back to the surface while remaining filament and coronal mass are ejected.

A solar filament eruption/CME on 2011 June 7 is one of the most well-studied solar filament eruptions (see Ref.[25,91] and references therein), and it is accompanied by an M2 class X-ray flare (its approximate energy is $\sim 10^{30}$ erg). This can be an excellent solar counterpart of stellar filament eruption on EK Dra. The dramatic filament eruption was mainly observed by EUV images (especially the 304 Å and 193 Å bands) and optical coronagraph. The fast components of the filament erupt with the velocity of 200-600 km s$^{-1}$ (ref.[25]), and much of the erupted filament material fell to the solar surface. On the other hand, some filamentary material and coronal masses have been observed to be ejecting as a CME with a velocity of $\sim$1000 km s$^{-1}$, which eventually reached at least 1 AU. Several aspects of this solar filament eruption described above are similar to those of the spectra of the EK Dra event.

We note that as for masses and kinetic energies in Fig. 4, a large number of CMEs are plotted while the number of filament eruptions/surges is only six (see Section "Velocity, mass, and kinetic energy: solar data"). The outer-region CMEs are often used for the statistical studies of solar mass ejections[2,90] while statistics of detailed physical parameters (such as masses and kinetic energies) of filament eruptions/surges are lacking and more studies are required.

**TESS pixel-level data analysis** Fig. S1 shows temporal variations of distance between EK Dra's sky location at each time and pre-flare location during the superflare based on the TESS pixel-level photometric data[12]. No centroid motion is observed during this flare (Fig. S1b), suggesting it is associated with the EK-Dra system rather than an instrumental systematic error or contamination from scattered background light or a distant star.

**Flare energy** The TESS white-light flare's bolometric energy is derived from the TESS light curve in the formula of[3,32]

$$E_{\rm bol} = \int_{\rm flare} \sigma_{\rm SB} T_{\rm flare}^4 A_{\rm flare} dt, \tag{1}$$

where the bolometric flare energy ($E_{\rm bol}$), the flare effective temperature ($T_{\rm flare}$), the area of flare ($A_{\rm flare}$), and the Stefan-Boltzmann constant ($\sigma_{\rm SB}$). For each time, the flare area is calculated based on the flare enhancement, flare effective temperature, stellar radius of 0.94 solar radius, and TESS response function[12]. The spectrum of white-light flares is assumed as a blackbody spectrum with the 10,000 K effective temperature. Although broadband optical spectra have never been observed for superflares on solar-type stars, the 10,000 K blackbody radiation is a good approximation for the M-dwarf stellar flares[100] or solar flares[101]. Even if the flare temperature becomes 6,000-7,000 K, the estimated energies become smaller only by a factor of 0.5. The H$\alpha$ flare energy is estimated from the enhanced H$\alpha$ E.W. and continuum flux level around H$\alpha$ line. The continuum flux of EK Dra around H$\alpha$ is derived as 1.57 W m$^{-2}$ nm$^{-1}$ ($\sim$ the solar value) at 1 astronomical unit for flux-calibrated spectra obtained by KOOLS-IFU with the stellar distance given by Gaia Data Release 2 (ref.[41]). HR7596 (A0III-type well-known standard star) is used for the flux calibrations as a standard star. The H$\alpha$ flux can contain errors of about a few % due to the difference in the air-mass conditions of HR7596 (1.402) and EK Dra (1.318). Then the H$\alpha$ energy is calculated by just multiplying the enhanced H$\alpha$ E.W. (integrated for H$\alpha$ - 10 Å $\sim$ H$\alpha$ + 10 Å) by the continuum flux and integrating in time.

**Relation between flares and spots on EK Dra** Fig. S2 shows the relation between flare radiated energy and spot size for each TESS-sector (14-16 and 21-23) on EK Dra. TESS photometry has detected 79 superflares with the an energy of more than $10^{33}$ erg during this campaign according to the automatic detection method[3]. We defined a flare index as the total flare radiated energy, which is the integrated radiated energy for all flares whose energy is more than $10^{33}$ erg during each TESS sector. The brightness modulation amplitude is responsible for the spot filling factor, which is derived as the difference between its brightness 95 % level and 5% level for each sector. Fig. S2 demonstrates a positive correlation between total flare radiated energy and brightness amplitude, signifying that the detected superflares are likely to occur associated with the prominent (or many) starspots on the solar-type stars EK Dra.

The magnetic energy stored around the giant starspots on EK Dra is estimated from the local brightness variation amplitude normalized by averaged stellar brightness ($\Delta F/F_{\rm av}$ = $(F_{\rm max} - F_{\rm min})/F_{\rm av}$) between BJD 2458945 to 2458947.5 (see Extended Data Fig. 1). Here $F_{\rm av}$, $F_{\rm max}$, and $F_{\rm min}$ mean average, maximum, and minimum value of stellar brightness of flare-subtracted light curves, respectively. The spot area (cf. filling factor) is derived to be 2.7 % of the stellar disk area $(= \pi R_*^2$ , where $R_*$ is the stellar radius) from the $\Delta F/F_{\rm av}$ in the same way as ref.[93]. The magnetic energy stored around the spot is calculated to be $8.0\times10^{35}$ erg from the spot area in the same way as ref.[4]:

$$E_{\rm mag} \approx 7\times10^{32}({\rm erg})\left(\frac{B}{10^3{\rm G}}\right)^2\left[\frac{A_{\rm spot}/(2\pi R_\odot^2)}{0.001}\right]^{\frac{3}{2}}, \quad (2)$$

where $B$ is the magnetic field strength, $A_{\rm spot}$ is the spot area, and $R_\odot$ is the solar radius. Here, we assumed the average magnetic field strength of star spots is $\sim$1000 G as in ref.[4]. Note that the estimated value can be a lower limit because there is no evidence that $F_{\rm max}$ corresponds to the unspotted brightness level.

**Spectroscopic data analysis (continued from Methods)** Fig. S3 shows the time-integrated flare spectra evolution during the events. The differences between blue- or red-shifted absorption components in the pre-flare and flare spectra are readily apparent in Fig. 1c-e (about 1.5 % at most). The far-wing continuum levels of flare spectra are well consistent with that of the pre-flare spectrum, indicating that the blue-shifted components are of astrophysical origin. In Fig. S4b and c, we made two light curves of the H$\alpha$ E.W. with the integration ranges of H$\alpha$ - 10 Å $\sim$ H$\alpha$ + 10 Å and H$\alpha$ - 20 Å $\sim$ H$\alpha$ + 10 Å, respectively. The narrow-band H$\alpha$ E.W. is used for the measurements of the radiated energy and duration of H$\alpha$ flare because of the high S/N (Fig. S4b), and the broad-band H$\alpha$ E.W. is used for the measurements of the amount of absorption (i.e., mass and kinetic energy) because the wavelength of $>$ H$\alpha$ - 20 Å is broad enough to measure the blue-shifted absorption features. The KOOLS-IFU and MALLS cover other chromospheric lines, such as He I lines at 6678.2 Å, but they are less sensitive to flares than H$\alpha$ as in M-dwarf flares[19], and no significant flare emission was obtained for this time.

**Stability of pre-flare spectra** Fig. S4 shows the extended light curve of the superflare and pre-flare brightness on EK Dra. The light curve shows that the pre-flare H$\alpha$ E.W. and continuum level are stable enough to detect the flare emission above the 1-$\sigma$ level in each. The 1-$\sigma$ levels were calculated based on the scattering of E.W. for -150 to 0 min before the flare onsets. The duration differences between the optical and H$\alpha$ flares were not significantly detected by considering the error bars in H$\alpha$ E.W.. Emission delays are seen in other stellar flare events, and the flare evolution on the different emission bands/lines should be investigated in future studies[94]. We obtained the pre-flare template spectra by averaging the 30 data points before the flare started. The periods used for the pre-flare spectra are indicated with black arrows in the Fig. S4a-b. 2-m Nayuta Telescope has a smaller mirror than 3.8-m Seimei Telescope, and it is necessary to use longer periods to make the pre-flare template spectrum. Fig. S5 shows temporal variations of the H$\alpha$ spectra in pre-flare phase on time scales similar to the filament eruption event. The panel shows that the pre-flare H$\alpha$

spectrum is quite stable for a significant amount of time before the flare event. Considering the sufficient stability of the E.W. in pre-flare phase, we can exclude that the observed variations in the H$\alpha$ profile could be due to background variations of the stellar chromosphere.

**Solar data analysis (continued from Methods)** Here, we introduce the continued description on the solar data analysis in Methods section "Solar data analysis". First, let us introduce why we used the data of partial regions although there are full-disk data of SDDI. It should be noted that if the length scale of the filament is much larger, the signals of filament eruptions are expected to be detected even with the full-disk integrated spectra. However, in this case, the ratio of $L(6570.8\text{Å}, t_0, A_{\rm local})$ to $L(6570.8\text{Å}, t_0, A_{\rm full-disk})$ is $\sim$2 %, and the absorption signals of the filament eruption are just about 0.01 % compared to the full-disk continuum level. In addition, there are slight time-lags among the 41-wavelength images observed by SDDI[15], and atmospheric scintillations and partial cloud would make the S/N ratio worse when we simply make the full-disk-integrated spectra. These are the reasons why we first made the locally-integrated spectra and then converted to the full-disk value.

Second, we describe below the detailed explanation of the solar filament eruption. In Extended Data Fig. 4c, the fast eruption can be seen in the second and third row (t = 1 min, 5 min), while the red-shifted component becomes dominant in the forth row (t = 11 min). This means that a fast eruption occurred but some of the erupted mass falls back toward the surface. It should be noted that there is flaring emission in the line center and the line center $\pm$ 1 Å even in the third to forth rows, although H$\alpha$ E.W. shows negative values compared to the pre-flare level. This means that the absorption due to erupted masses is dominant compared to the flare emission in the decay phase, which is similar to the stellar filament eruption (Fig. 1). The absorption from ejected mass is very weak in the line center due to low contrast in line center against the weak background intensity. The weak absorption can be also filled in the continuing H$\alpha$ flaring component (see Extended Data Fig. 4c). This feature at line center cannot be seen in stellar spectra possibly because of the lack of the spectral resolution (10 times worse than solar spectra).

Finally, we describe whether it has become a CME. Ref.[42] reported that the filament eruption analyzed here could have produced a CME on the basis of the coronagraph observed by the Large Angle and Spectrometric Coronagraph (LASCO) C2 images onboard the Solar and Heliospheric Observatory (SOHO)[102] . The running difference movies can be seen in Fig. S6c (see the movie in the url: `https://cdaw.gsfc.nasa.gov/movie/make_htmem_js.php?step=1&img1=lasc2rdf&stime=20160707_0000&etime=20160707_2359`). The plane-of-sky distance from the solar disk center of filament eruption and corresponding CMEs are plotted in Fig. S6a-b. The filament height is measured as the farthest filament components from the disk center. The CMEs have the two components, and the evolution of both components are indicated with orange and green points/arrow in Fig. S6a and Fig. S6c. Ref.[42] shows that the directions of filament eruption and CME propagation are roughly the same, and Fig. S6 shows that the CME height evolution is roughly consistent with the timing when the filament eruption occurred. Although the large part of filaments have fallen back to the Sun (see Supplementary Video1), the extended regions of the coronal mass may have led to the CMEs.

**Velocity, mass, and kinetic energy: solar data** For solar filament eruption observed with SMART/SDDI, we applied the Becker's cloud-model fitting, and derived the surface distributions of mass of erupted filament at 7 July 2016 07:56:09UT. Fig. S7 shows the detailed result of the could-model fitting for the filament eruption. The detailed methods of the cloud model are described in previous studies[26,48]. As a result of the fitting, the mean radial velocity is $-61$ km s$^{-1}$, source function is 0.28, and velocity dispersion of 38 km s$^{-1}$ with the mean optical thickness of 0.69. The estimated values of almost all points are in good agreements with the previous studies[48]. The distribution of the hydrogen column density is derived from the optical depth and its spatial scale of $2.2\times10^{9}$ cm[51]. The plasma mass and kinetic energy are then calculated as $1.3\times10^{15}$ g and $7.7\times10^{28}$ erg, respectively. The kinetic energy is the lower limit because we only considered the line-of-sight velocity, which is sufficient to compare with stellar events. For a comparison with the stellar filament mass estimation, we calculated the mass for the solar filament eruption only from the spatially-integrated H$\alpha$ E.W. of $2.9\times10^{-4}$ Å (Fig. 2a) under the same assumption of the stellar data. As a result, the mass derived only from the H$\alpha$ light curve is estimated to be $3.3\times10^{15}$ g, which is in good agreement with that derived from spatially-resolved analysis within the above model errors (0.15-4.9). This validates our model to estimate the stellar filament mass.

As for the other solar filament/prominence eruptions and surges plotted in Fig. 4, the mass, kinetic energies of solar erupting plasma are also plotted whose data are taken from previous studies[43–46]. The data and references are summarized in Table 1. Note that we have analyzed another solar eruptive event ("Event-2") and the analysis is introduced in section "Another case of solar flares on 2 April 2017". For these flares, we assumed that bolometric energies of B, C, and M class solar flares are $10^{28}$, $10^{29}$, and $10^{30}$ erg from observational estimates of solar flare energies[33,47,101]. The statistical studies of the relation among prominence mass, prominence kinetic energy, and flare energy are now lacking, and more Balmer-lines observations of solar prominence eruptions will be helpful for understanding stellar events.

**Another case of solar flares on 2 April 2017** In addition to the solar flare and filament eruption on 7 July 2016 (hereafter "Event-1"), we analyzed a C8.0-class solar flare (i.e., the peak GOES soft X-ray flux $F_{\rm GOES}$ is $8.0\times10^{-6}$ W m$^{-2}$) and associated jet-like filament eruption (called solar "surge") on 02:46 UT observed by the SDDI (hereafter "Event-2"). Our purpose here is to show another example of solar cool-mass eruption associated with solar flares. The Event-2 was analyzed in the same way as Event-1. It should be noted that it takes full-disk solar images at 73 wavelength points at every 0.25 Å (cf. 0.5 Å for Event-1) from the H$\alpha$ line center $-9.0$ Å to the H$\alpha$ line center +9.0 Å, and the time cadence is 15 seconds (cf. 20 seconds for Event-1). The C8.0-class solar flare is the largest solar flare with cool-mass eruption (filament eruptions or surges) among the events observed by SDDI with good weather condition in these 5 years. The full movie of the solar flare and surge observed by the SMART telescope/SDDI at Hida Observatory is shown in Supplementary Video2.

Before going to the detailed analysis, we will explain the meaning of filament eruptions and surges, as used in solar physics. During solar flares, the associated cool eruptive phenomena seen in H$\alpha$ are observationally classified to two classes: "filament eruptions" (typically having large scales) and "surges" (having small scales). Although they were historically named based on the observational visibility, both of them are often associated with flares and sometimes cause the outer-region CMEs[2,99]. Some of the solar surges do not erupt far away from the surface[96,97] but others with high velocity lead to the CMEs[98] with velocities higher than the solar escape velocity[99]. This is also the same for large-scale filament eruptions. Theoretically, both surges and filament eruptions can be explained by the unified model of magnetic reconnection with filament although the length scales are different[1,95]. Event-2 was also sufficient for analyzing the H$\alpha$ behaviors of solar cool eruptive phenomena and confirming whether the stellar H$\alpha$ spectral changes correspond to the similar phenomena.

Fig. S8 and Fig. S9 correspond to the same figures as Extended Data Fig. 4 and Fig. 2, respectively, but for the Event-2. This flare occurred around an active region, named "NOAA 12645", located around solar disk center and was accompanied by solar surge. We found that the blue-shifted absorption component at several times 10 km s$^{-1}$ due to the surge was predominant after the solar flare, and the spatially integrated H$\alpha$ E.W. showed enhanced absorption (Fig. S9a). Later, the blue-shifted component decelerated and gradually turned into slow, red-shifted absorption (Fig. S9b-c). The H$\alpha$ E.W. returned to the pre-flare level in about 30 min (Fig. S9a). These features are very similar to the case of Event-1.

The drifted components in time-velocity plane seen in Fig. S9b can be caused by the free-falling under the gravity gradient and the change in visibility of the dominant plasma caused by the disappearance of the initial fast component. This feature is very similar to the stellar flare events in Fig. 1.

For the solar surge observed with SMART/SDDI, we applied Becker's cloud-model fitting, and derived the surface distributions of ejected mass at a given time of 2 April 2017 03:18:59UT. Fig. S10 shows the detailed result of the could-model fitting for the solar surge. As a result of the fitting, the $\tau$-weighted radial velocity is $-31$ km s$^{-1}$, source function is 0.22, and velocity dispersion of 18 km s$^{-1}$ with the mean optical thickness of 0.73. The plasma mass and kinetic energy are then calculated as $5.1\times10^{14}$ g and $8.5\times10^{27}$ erg, respectively (see Table 1).

**Solar flare energy - CME mass relation** In Fig. 4, the data of CME mass and kinetic energy as a function of flare energy are plotted[29]. The flare energies are originally given by GOES X-ray energies in 1-8 Å ($E_{\rm X,GOES}$), and they are converted to the bolometric energies under the assumption of $100 \times E_{\rm X,GOES}$. This is because the statistical study of solar flares shows that the GOES X-ray band radiates only 1 % of the bolometric energy (≈white-light energy)[47]. The relation between CME mass and flare energy are empirically derived as $M \propto E^{0.59\pm0.02}$ (ref.[29]), where $M$ is CME mass. On the other hand, the relation between mass and peak GOES X-ray flux (that is, the best-used flare energy scale) has been reported by the different authors[28]. The relation between mass and flare energy are empirically derived as $M \propto E^{0.7\pm0.05}$ (ref.[28]) under the assumption that bolometric energies of B, C, and M class solar flares are $10^{28}$, $10^{29}$, and $10^{30}$ erg[33,47,101]. Both scaling laws are plotted in Fig. 4a, although the plotted data are taken from ref.[29] here. Stellar ejected mass is well described by the latter scaling law[28] but is relatively more massive than expected from the former scaling law[29]. Theoretically, the relation between mass and flare energy is derived as $M \propto E^{2/3}$ (ref.[30]). which is consistent with both scaling laws. It should be noted that there is large scatter in the solar data. When we apply the solar scaling laws to superflare discussions, we only take into account the fitting error in the original solar studies ref.[28,29]. The results and discussions can be adjusted when the samples of solar CMEs are increased in the future studies.

**Relation between magnetic field structure of EK Dra and the filament eruption** Some studies with the Doppler imaging technique showed that there are large star spots around the equator without any polar spots from the observation data in 2015[103], and ref.[9] reported that there is a small polar spot from the observation data in 2015[9]. The polar spot may be related to a possible strong large-scale dipole magnetic field. Zeeman Doppler imaging of EK Dra showed that mean surface magnetic field strength is 66-89 G during 2007-2012[9].

It is proposed that the large-scale overlaying strong magnetic fields can suppress the stellar mass ejections[27]. Ref.[27] simulated stellar mass ejections under the large scale magnetic field of 75 G and proposed that the particular large-scale magnetic field configuration establishes a suppression threshold around $\sim 3\times10^{32}$ erg in the kinetic energy of mass ejections. Although the similar large scale field is not always prominent for EK Dra as mentioned above, the assumed magnetic field strength $\sim$75 G is similar to the past observations of 66-89 G on EK Dra. If we simply apply the simulation result to our observation, the observed kinetic energy of EK Dra eruption $3.5\times10^{32}$ erg is comparable to the suppression threshold $\sim 3\times10^{32}$ erg. This may mean that the ejected mass have a potential to escape from the magnetic field suppression, although they can significantly lose the kinetic energy. It seems to suggest that only superflares on active solar-type stars might have associated CMEs, with the far more numerous weaker flares representing fully confined eruptions.

However, there are no magnetic field maps covering our observation period. The maps of magnetic field and spots depend on the observational periods[9,103] that are probably due to new spot emergence/decay, long-term stellar activity cycles, or stellar differential rotations.

As in the description of "TESS light-curve analysis", the superflare occurred near the local brightness maximum, although some of the starspots are expected to be visible from the observer[9,34–36,40]. This may mean that the erupted mass was not suppressed by the strong overlaying "local" magnetic field of large spots.

**Low mass companion** Although a faint low-mass companion is reported about 20 AU away from EK-Dra solar-type primary star (projected distance)[104], they are believed to be not magnetically coupled[9]. X-ray[11,105] and UV[10] stellar flares have been observed on EK Dra so far, and they are thought to occur on the solar-type primary star. The absorption of the blue-shift component is 1.5 % of the continuum level (Fig. 1e) while the low-mass companion is about six magnitudes fainter in V-band compared to the solar-type primary star[104]; therefore it is unlikely to be explained by the low-mass companion even if the whole continuum levels of the companion star is absorbed. Also, the hypothesis that the filament eruption generated on the low-mass companion passed the solar-type primary star and produced the absorption can be rejected considering the difference between the traveling timescale across the projected distance of 20 AU and the short time lag between flares and filament eruption phenomenon.

Also, the rotational brightness variations would be caused by the solar-type primary star, considering the luminosity differences (Extended Data Fig. 1). The total flare radiated energies are positively related to the spot filling factor changes measured for each TESS observational sector (Fig. S2), indicating that superflares are also related to the solar-type primary star.

**Future works** Here, we mention future directions of our work in more detail. Although it should be noted that the following discussion is just speculation at present, future works may give important insights into the following points: impact of stellar CMEs on (1) stellar mass loss evolution and (2) planetary atmospheric evolution.

First, let us summarize its impact on stellar mass loss. Ref.[7] calculated the mass loss rate due to CMEs as $2{\times}10^{-12}$ $M_{\odot}$ yr$^{-1}$ - $9{\times}10^{-13}$ $M_{\odot}$ yr$^{-1}$ by assuming that all stellar flares are associated with stellar CMEs. This mass loss rate is 50-100 times larger than the solar value $\sim$$2{\times}10^{-14}$ $M_{\odot}$ yr$^{-1}$ (ref.[106]). It should be noted that ref.[7] used the X-ray flare occurrence frequency of EK Dra of $\sim$4.2 flares d$^{-1}$ (at 1995, ref.[11]), which is significantly larger than that obtained by TESS photometry $\sim$0.5 flares d$^{-1}$ (at 2019-2020). This can possible be due to the difference in phase of the activity cycle or the energy partition among the X-ray and optical wavelengths. The mass-loss rate estimated from TESS photometry is $\sim$10 times smaller than that from ref.[7], but it is still $\sim$5-10 times larger than the solar value. Likewise, ref.[107,108] predicted stellar mass-loss rates of hundreds of times the solar values solely due to CMEs. However, since not all flares may produce CMEs, the above estimation is just speculation. For M-dwarfs, it is reported that the mass-loss rates obtained via Ly$\alpha$ absorption are much smaller than expected CME mass loss rates (ref.[108] and references therein), which may mean that CMEs are rare for active stars due to the confinement of eruptions. Again, the values of mass loss rate presented above are just speculation. In order to clarify this point, we need to continue the monitoring observations of filament eruptions/CMEs on solar-type stars and clarify the occurrence frequency of CMEs in the future.

Second, it has been speculated that the filament eruptions/CMEs associated with superflares can severely affect exoplanetary atmospheres (see ref.[6] for review). For example, it is proposed that high-energy particles associated with stellar CMEs can contribute to generation of greenhouse gases or prebiotic compounds [6,89]. This may be related to the planetary habitability around young stars including the young Sun. This aspect can greatly influence the theory of origins of life on planets. In addition, it was recently reported that not only the young Sun but also the present-day Sun could produce superflares from observations of solar-type stars[3,5,32,36,109,110]. The possible association of CMEs may significantly impact both kinds of solar-system planetary environments. Numerical simulations of stellar CMEs have improved in recent years [6,27], and by comparing these with observational data, we will be able to evaluate these broader impacts in more detail.


1. Shibata, K. & Magara, T. Solar Flares: Magnetohydrodynamic Processes. *Living Rev. Sol. Phys.*, **8**, 6 (2011).

2. Gopalswamy, N. et al., Prominence Eruptions and Coronal Mass Ejection: A Statistical Study Using Microwave Observations. *Astrophy. J*, **586**, 562 (2003).

3. Maehara, H. et al. Superflares on Solar-type stars. *Nat.*, **485**, 478-481 (2012).

4. Shibata, K. et al., Can Superflares Occur on Our Sun?. *Publ. Astron. Soc. Jpn.*, **65**, 49 (2013).

5. Notsu, Y. et al., Do Kepler Superflare Stars Really Include Slowly Rotating Sun-like Stars? — Results Using APO 3.5 m Telescope Spectroscopic Observations and Gaia-DR2 Data. *Astrophy. J*, **876**, 58 (2019).

6. Airapetian, V. S. et al., Impact of space weather on climate and habitability of terrestrial-type exoplanets. *Int. J. Astrobiol.*, **19**, 136 (2020).

7. Osten, R. A. & Wolk, S. J. Connecting Flares and Transient Mass-loss Events in Magnetically Active Stars. *Astrophy. J*, **809**, 79 (2015).

8. Miyake, F. et al. A signature of cosmic-ray increase in AD 774-775 from tree rings in Japan. *Nat.* 486, 240-242. (2012).

9. Waite, I. A. et al., Magnetic fields on young, moderately rotating Sun-like stars - II. EK Draconis (HD 129333). *Mon. Not. R. Astron. Soc.*, **465**, 2076 (2017).

10. Ayres, T. R., The Flare-ona of EK Draconis. *Astrophy. J*, **150**, 7 (2015).

11. Audard, M., Güdel & M., Guinan, E. F., Implications from Extreme-Ultraviolet Observations for Coronal Heating of Active Stars. *Astrophy. J*, **513**, L53 (1999).

12. Ricker, G. R. et al. Transiting Exoplanet Survey Satellite (TESS). *J. Astron. Telesc. Instrum. Syst.*, **1**, 014003 (2014).

13. Kurita, M. et al., The Seimei telescope project and technical developments. *Publ. Astron. Soc. Jpn.*, **72**, 48 (2020).

14. Schmieder, B. et al., Evidence for Gentle Chromospheric Evaporation during the Gradual Phase of Large Solar Flares. *Astrophy. J*, **317**, 956 (1987).

15. Ichimoto, K. et al., A New Solar Imaging System for Observing High-Speed Eruptions: Solar Dynamics Doppler Imager (SDDI). *Sol. Phys.*, **292**, 63 (2017).

16. Švestka, Z., Kopecký, M. & Blaha, M., *Bull. Astron. Inst. Czechoslov.* **13**, 37 (1962).

17. Ichimoto, K. & Kurokawa, H. H$\alpha$ Red Asymmetry of Solar Flares. *Sol. Phys.*, **93**, 105 (1984).

18. Houdebine, E. R., Foing, B. H. & Rodono, M. Dynamics of flares on late-type dMe stars. I. Flare mass ejections and stellar evolution. *Astron. Astrophys.*, **238**, 249 (1990).

19. Honda, S. et al., Time-resolved spectroscopic observations of an M-dwarf flare star EV Lacertae during a flare. *Publ. Astron. Soc. Jpn.*, **70**, 62 (2018).

20. Leitzinger, M., et al., Search for indications of stellar mass ejections using FUV spectra. *Astron. Astrophys.*, **536**, A62 (2011)

21. Vida, K. et al., Investigating magnetic activity in very stable stellar magnetic fields. Long-term photometric and spectroscopic study of the fully convective M4 dwarf V374 Pegasi. *Astron. Astrophys.* **590**, A11 (2016).

22. Argiroffi, C. et al., A stellar flare-coronal mass ejection event revealed by X-ray plasma motions. *Nat. Astron.*, **3**, 742 (2019).

23. Veronig, A. M. et al., Indications of stellar coronal mass ejections through coronal dimmings. *Nat. Astron.*, online (2021).

24. Moschou, S.-P. et al., The Stellar CME-Flare Relation: What Do Historic Observations Reveal?. *Astrophy. J*, **877**, 105 (2019).

25. Wood, B. E., Howard, R. A., & Linton, M. G., Imaging Prominence Eruptions out to 1 AU. *Astrophy. J.* **816**, 67, (2016)

26. Seki, D. et al., Relationship between three-dimensional velocity of filament eruptions and CME association, *Earth, Planets, and Space*, **73**, 58 (2021)

27. Alvarado-Gómez, J. D. et al., Suppression of Coronal Mass Ejections in Active Stars by an Overlying Large-scale Magnetic Field: A Numerical Study. *Astrophy. J*, **862**, 93 (2018).

28. Aarnio, A. N., Matt, S. P., Stassun & K. G. Mass Loss in Pre-main-sequence Stars via Coronal Mass Ejections and Implications for Angular Momentum Loss. *Astrophy. J*, **760**, 9 (2012).

29. Drake, J. J. et al. Implications of Mass and Energy Loss due to Coronal Mass Ejections on Magnetically Active Stars. *Astrophy. J*, **764**, 170 (2013).

30. Takahashi, T., Mizuno, Y. & Shibata, K. Scaling Relations in Coronal Mass Ejections and Energetic Proton Events Associated with Solar Superflares, *Astrophy. J*, **833**, L8 (2016).

31. Fausnaugh, M. M. et al. TESS Data Release Notes: Sector 23, DR32, (2020)

32. Shibayama, T. et al. Superflares on Solar-type Stars Observed with Kepler. I. Statistical Properties of Superflares. *Astrophy. J. Supplement Series*, **209**, 5, (2013)

33. Namekata, K. et al. Statistical Studies of Solar White-light Flares and Comparisons with Superflares on Solar-type Stars. *Astrophy. J*, *851*, 91, (2017)

34. Roettenbacher, R. M., Vida, K., The Connection between Starspots and Flares on Main-sequence Kepler Stars. *Astrophy. J.* **868**, 3, (2018)

35. Doyle, L., et al., Investigating the rotational phase of stellar flares on M dwarfs using K2 short cadence data. *Mon. Not. R. Astron. Soc.* **480**, 2153-2164, (2018)

36. Doyle, L., Ramsay, G., & Doyle, J. G., Superflares and variability in solar-type stars with TESS in the Southern hemisphere. *Mon. Not. R. Astron. Soc.* **494**, 3596-3610, (2020)

37. Namekata, K., et al., Temporal Evolution of Spatially Resolved Individual Star Spots on a Planet-hosting Solar-type Star: Kepler-17. *Astrophy. J.* **891**, 103 (2020)

38. Matsubayashi, K. et al. KOOLS-IFU: Kyoto Okayama Optical Low-dispersion Spectrograph with optical-fiber Integral Field Unit. *Publ. Astron. Soc. Jpn*, **71**, 102 (2019).

39. Ozaki, S. & Tokimasa, N. The optical spectrograph for the NAYUTA telescope I. Design. *Annual Report of the Nishi-Harima Astronomical Observatory (ISSN 0917-6926)*, **15**, 15-29 (2005)

40. Namekata, K. et al. Optical and X-ray observations of stellar flares on an active M dwarf AD Leonis with the Seimei Telescope, SCAT, NICER, and OISTER. *Publ. Astron. Soc. Jpn*, **72**, 68, (2020).

41. Gaia Collaboration et al. Gaia Data Release 2. Summary of the contents and survey properties. *Astron. Astrophys.*, **616**, A1, (2018)

42. Seki, D. et al., SMART/SDDI Filament Disappearance Catalogue. *Sun and Geosphere* **14**, 95, (2019)

43. Jain, R. & Sorathia, B. Flare-associated surge prominence on 1980 October 30. *Astron. Astrophys.*, **8**, 295 (1987).

44. Liu, Y. & Kurokawa, H. On a Surge: Properties of an Emerging Flux Region. *Astrophy. J*, **610**, 1136 (2004).

45. Ohyama, M. & Shibata, K. X-ray Plasma Ejection Associated with H$\alpha$ Filament Eruption. *Solar Physics with Radio Observations, Proceedings of the Nobeyama Symposium*, **479**, 367-370 (1998).

46. Christian, D. J. et al., H$\alpha$ and EUV Observations of a Partial CME. *Astrophy. J*, **804**, 147 (2015).

47. Emslie, A. G. et al., Global Energetics of Thirty-eight Large Solar Eruptive Events. *Astrophys. J.*, **759**, 71 (2012).

48. Sakaue, T. et al. Observational study on the fine structure and dynamics of a solar jet. II. Energy release process revealed by spectral analysis. *Publ. Astron. Soc. Jpn.*, **70**, 99, (2018)

49. Mein, P. & Mein, N. Differential cloud models for solar velocity field measurements. *Astron. Astrophys.*, **203**, 162, (1988)

50. Odert, P. et al., Stellar coronal mass ejections - II. Constraints from spectroscopic observations. *Mon. Not. R. Astron. Soc.*, **494**, 3766 (2020).

51. Tsiropoula, G. & Schmieder, B. Determination of physical parameters in dark mottles. *Astron. Astrophys.*, **324**, 1183 (1997).

52. Flores Soriano, M. & Strassmeier, K. G., Short-term evolution and coexistence of spots, plages and flare activity on LQ Hydrae. *Astron. Astrophys.*, **597**, A101 (2017)

53. Vida, K., et al., The quest for stellar coronal mass ejections in late-type stars. I. Investigating Balmer-line asymmetries of single stars in Virtual Observatory data. *Astron. Astrophys.*, **623**, A49 (2019)

54. Gunn, A. G. et al., High-velocity evaporation during a flare on AT Microscopii. *Astron. Astrophys.*, **285**, 489 (1994).

55. Fuhrmeister, B. & Schmitt, J. H. M. M. Detection and high-resolution spectroscopy of a huge flare on the old M 9 dwarf DENIS 104814.7-395606.1. *Astron. Astrophys.*, **420**, 1079 (2004).

56. Fuhrmeister, B., et al., Multiwavelength observations of a giant flare on CN Leonis. I. The chromosphere as seen in the optical spectra. *Astron. Astrophys.*, **487**, 293, (2008)

57. Leitzinger, M. et al., A search for flares and mass ejections on young late-type stars in the open cluster Blanco-1. *Mon. Not. R. Astron. Soc.* **443**, 898-910 (2014).

58. Korhonen, H. et al., Hunting for Stellar Coronal Mass Ejections. *Living Around Active Stars, Proceedings of the International Astronomical Union, IAU Symposium* **328**, 198-203 (2017).

59. Muheki, P. et al., Properties of flares and CMEs on EV Lac: possible erupting filament. *Mon. Not. R. Astron. Soc.* **499**, 5047-5058 (2020)

60. Maehara, H., et al., Time-resolved spectroscopy and photometry of M dwarf flare star YZ Canis Minoris with OISTER and TESS: Blue asymmetry in the H α line during the non-white light flare. *Publ. Astron. Soc. Jpn.* **73**, 44 (2021)

61. Zic, A., et al., A Flare-type IV Burst Event from Proxima Centauri and Implications for Space Weather. *Astrophy. J.*, **905**, 23 (2020)

62. Guenther, E. W., Emerson, J. P., Spectrophotometry of flares and short time scale variations in weak line, and classical T Tauri stars in Chamaeleon. *Astron. Astrophys.* **321**, 803-810 (1997).

63. Haisch, B. M., et al., Coordinated Einstein and IUE observations of a disparitions brusques type flare event and quiescent emission from Proxima Centauri. *Astrophy. J.*, **267**, 280 (1983)

64. Ottmann, R. & Schmitt, J. H. M. M., ROSAT observation of a giant X-ray flare on Algol: evidence for abundance variations? *Astron. Astrophys.*, **307**, 813 (1996)

65. Wheatley, P. J., ROSAT observations of V471 Tauri, showing that stellar activity is determined by rotation, not age. *Mon. Not. R. Astron. Soc.*, **297**, 1145 (1998)

66. Tsuboi, Y. et al., ASCA Detection of a Superhot 100 Million K X-Ray Flare on the Weak-Lined T Tauri Star V773 Tauri. *Astrophy. J*, **503**, 894 (1998).

67. Favata, F. & Schmitt, J. H. M. M. Spectroscopic analysis of a super-hot giant flare observed on Algol by BeppoSAX on 30 August 1997. *Astron. Astrophys.*, **350**, 900 (1999).

68. Franciosini, E., et al., BeppoSAX observation of a large long-duration X-ray flare from UX Arietis. *Astron. Astrophys.*, **375**, 196 (2001)

69. Pandey, J. C. & Singh, K. P., A study of X-ray flares - II. RS CVn-type binaries. *Mon. Not. R. Astron. Soc.*, **419**, 1219 (2012)

70. Ambruster, C. W., et al., An episode of mass expulsion from the M-dwarf flare star EV Latertae ? *New Insights in Astrophysics*, **263**, 137 (1986)

71. Bond, H. E., et al., Hubble Space Telescope Imaging of the Outburst Site of M31 RV. II. No Blue Remnant in Quiescence. *Astrophy. J.*, **560**, 919 (2001)

72. Parsons, S. G., et al., Eclipsing post-common envelope binaries from the Catalina surveys. *Mon. Not. R. Astron. Soc.*, **429**, 256 (2013)

73. Leitzinger, M., et al., A census of coronal mass ejections on solar-like stars. *Mon. Not. R. Astron. Soc.*, **493**, 4570 (2020)

74. Leitzinger, M., et al., Stellar activity at FUV/Radio wavelengths. *Central European Astrophysical Bulletin*, **34**, 123 (2010)

75. Boiko, A. I., et al., Search of the radio emission from flare stars at decameter wavelengths. *Advances in Astronomy and Space Physics*, **2**, 121 (2012)

76. Villadsen, J., Hallinan, G., & Bourke, S., Radio spectroscopy of stellar flares: magnetic reconnection & CME shocks in stellar coronae. *Solar and Stellar Flares and their Effects on Planets*, **320**, 191 (2016)

77. Crosley, M. K., et al., The Search for Signatures of Transient Mass Loss in Active Stars. *Astrophy. J.*, **830**, 24 (2016)

78. Crosley, M. K. & Osten, R. A., Constraining Stellar Coronal Mass Ejections through Multi-wavelength Analysis of the Active M Dwarf EQ Peg. *Astrophy. J.*, **862**, 113 (2018)

79. Crosley, M. K. & Osten, R. A., Low-frequency Radio Transients on the Active M-dwarf EQ Peg and the Search for Coronal Mass Ejections. *Astrophy. J.*, **856**, 39 (2018)

80. Villadsen, J. & Hallinan, G. , et al., Ultra-wideband Detection of 22 Coherent Radio Bursts on M Dwarfs, *Astrophy. J.*, **871**, 214 (2019)

81. Allred, J. C. et al., Radiative Hydrodynamic Models of the Optical and Ultraviolet Emission from Solar Flares. *Astrophy. J*, **630**, 573 (2005).

82. Tei, A., Sakaue, T., Okamoto, T. J., et al., Blue-wing enhancement of the chromospheric Mg II h and k lines in a solar flare. *Publ. Astron. Soc. Jpn.* **70**, 100, (2018)

83. Kuridze, D., Mathioudakis, M., Simões, P. J. A., et al., H$\alpha$ Line Profile Asymmetries and the Chromospheric Flare Velocity Field *Astrophy. J*, **813**, 125, (2015)

84. Heinzel, P., Karlicky, M., Kotrc, P., et al., On the Occurrence of Blue Asymmetry in Chromospheric Flare Spectra. *Solar Physics*, **152**, 393, (1994)

85. Schwartz, P. et al., Prominence Visibility in Hinode/XRT Images. *Astrophy. J*, **807**, 97 (2015).

86. Osten, R. A. & Wolk, S. J. A Framework for Finding and Interpreting Stellar CMEs. *Living Around Active Stars, Proceedings of the International Astronomical Union, IAU Symposium*, **328**, 243-251 (2017).

87. Giampapa, M. S., et al., A preflare diminution in the quiescent flux of EQ Pegasi. *Astrophy. J. L.*, **252**, L39 (1982)

88. Doyle, J. G. & Collier Cameron, A., Mass ejections from the rapidly rotating M dwarf star GL 890. *Mon. Not. R. Astron. Soc.*, **244**, 291 (1990)

89. Airapetian, V. S. et al., Prebiotic chemistry and atmospheric warming of early Earth by an active young Sun. *Nat. Geosci.* **9**, 452-455 (2016).

90. Webb, D. F. & Howard, T. A., Coronal Mass Ejections: Observations. *Living Reviews in Solar Physics* **9**, 3, (2012)

91. Petralia, A., Reale, F., Orlando, S., et al., Bright Hot Impacts by Erupted Fragments Falling Back on the Sun: Magnetic Channelling. *Astrophy. J.* **832**, 2, (2016)

92. Aschwanden, M. J. & Gopalswamy, N., Global Energetics of Solar Flares. VII. Aerodynamic Drag in Coronal Mass Ejections. *Astrophy. J.* **877**, 149, (2019)

93. Maehara, H., et al., Starspot activity and superflares on solar-type stars. *Publ. Astron. Soc. Jpn.* **69**, 41 (2017)

94. Flaccomio, E. et al., A multi-wavelength view of magnetic flaring from PMS stars. *Astron. Astrophys.* **620**, A55. (2018)

95. Shibata, K., Evidence of Magnetic Reconnection in Solar Flares and a Unified Model of Flares. *Astrophysics and Space Science* **264**, 129-144, (1999)

96. Wang, R. et al., Sympathetic Solar Filament Eruptions. *Astrophy. J. Letters* **827**, L12, (2016)

97. Kayshap, P., Srivastava, A. K., & Murawski, K., The Kinematics and Plasma Properties of a Solar Surge Triggered by Chromospheric Activity in AR11271. *Astrophy. J.*, **763**, 24 (2013).

98. Liu, Y. et al., Observations of an Emerging Flux Region Surge: Implications for Coronal Mass Ejections Triggered by Emerging Flux. *Astrophy. J.* **628**, 1056-1060 (2005)

99. Liu, Y., A Study of Surges: II. On the Relationship between Chromospheric Surges and Coronal Mass Ejections. *Solar Physics* **249**, 75-84, (2008)

100. Hawley, S. L. & Fisher, G. H. X-Ray–heated Models of Stellar Flare Atmospheres: Theory and Comparison with Observations. *Astrophy. J. Supplement Series*, **78**, 565, (1992)

101. Kretzschmar, M. et al. The effect of flares on total solar irradiance. *Nat. Phys.*, **6**, 690-692, (2010)

102. Brueckner, G. E. et al., The Large Angle Spectroscopic Coronagraph (LASCO). *Solar Physics* **162**, 357, (1995)

103. Järvinen, S. P. et al., Mapping EK Draconis with PEPSI. Possible evidence for starspot penumbrae. *Astron. Astrophys.* **620**, A162 (2018).

104. König, B. et al. The young active binary star EK Draconis. *Astron. Astrophys.*, **435**, 215 (2005).

105. Telleschi, A. et al., Coronal Evolution of the Sun in Time: High-Resolution X-Ray Spectroscopy of Solar Analogs with Different Ages. *Astrophy. J*, **622**, 653 (2005).

106. Cohen, O., The independency of stellar mass-loss rates on stellar X-ray luminosity and activity level based on solar X-ray flux and solar wind observations. *Mon. Not. R. Astron. Soc.* **417**, 2592, (2011)

107. Odert, P., Leitzinger, M., Hanslmeier, A., et al., Stellar coronal mass ejections - I. Estimating occurrence frequencies and mass-loss rates. *Mon. Not. R. Astron. Soc.* **472**, 876, (2017)

108. Wood, B. E., Müller, H.-R., Redfield, S., et al. New Observational Constraints on the Winds of M dwarf Stars. *Astron. Astrophys.* **915**, 37, (2021)

109. Tu, Z.-L., Yang, M., Zhang, Z.J., et al., Superflares on Solar-type Stars from the First Year Observation of TESS. *Astrophy. J.* **890**, 46, (2020)

110. Tu, Z.-L., Yang, M., Wang, H.-F., et al., Superflares, Chromospheric Activities, and Photometric Variabilities of Solar-type Stars from the Second-year Observation of TESS and Spectra of LAMOST. *Astrophy. J. Suppl.* **253**, 35, (2021)

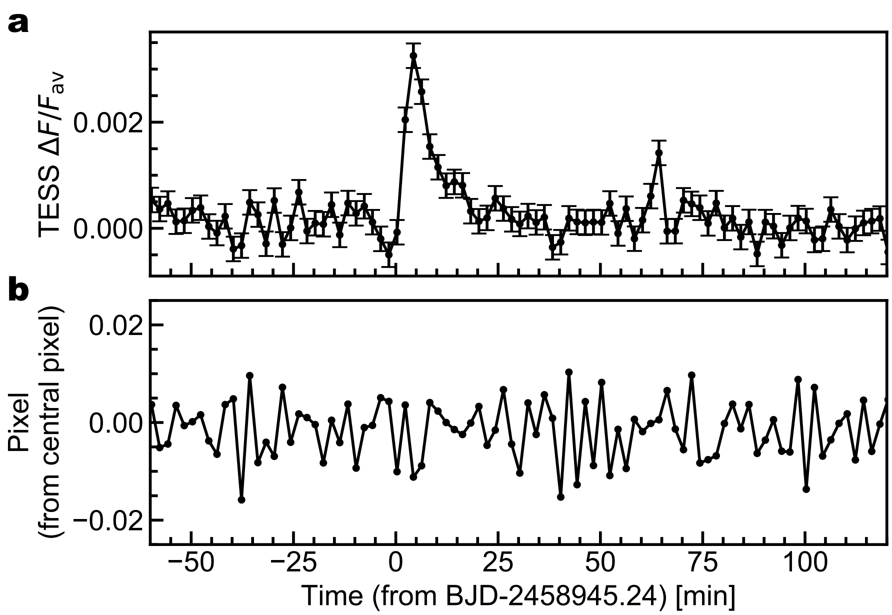


**Supplementary Fig. 1: Light curve and count-weighted central pixel variation during the superflare on EK Dra. (a)** Optical light curve of the superflare observed by TESS. **(b)** Count-weighted central pixel variation during the superflare.

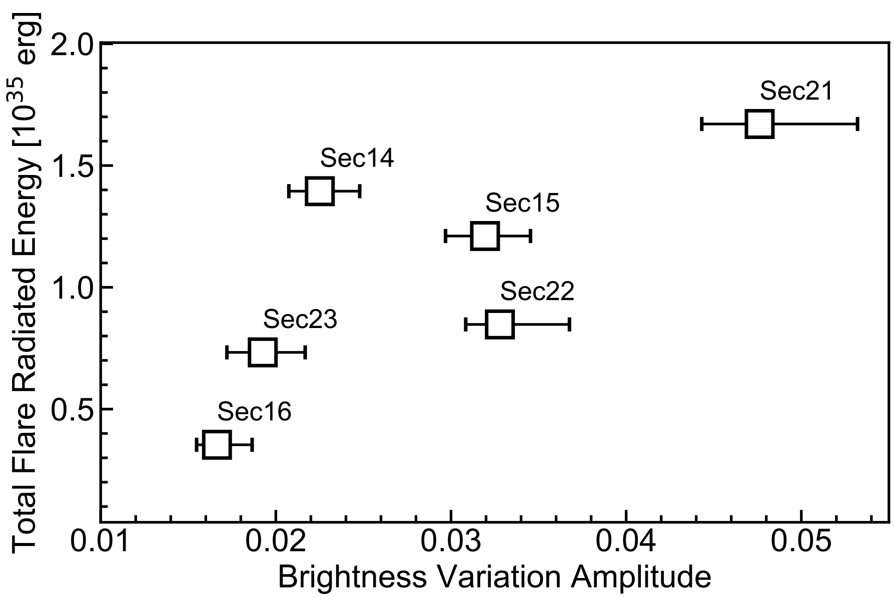


**Supplementary Fig. 2: Total flare radiated energy v.s. brightness variation amplitude on EK Dra.** The total flare radiated energy represents the integrated radiated energy for all flares whose energy is more than $10^{33}$ erg during each TESS sector. The brightness modulation amplitude is normalized by the stellar averaged luminosity and it is derived as the difference between its top 95 % and 5% brightness level for each sector.

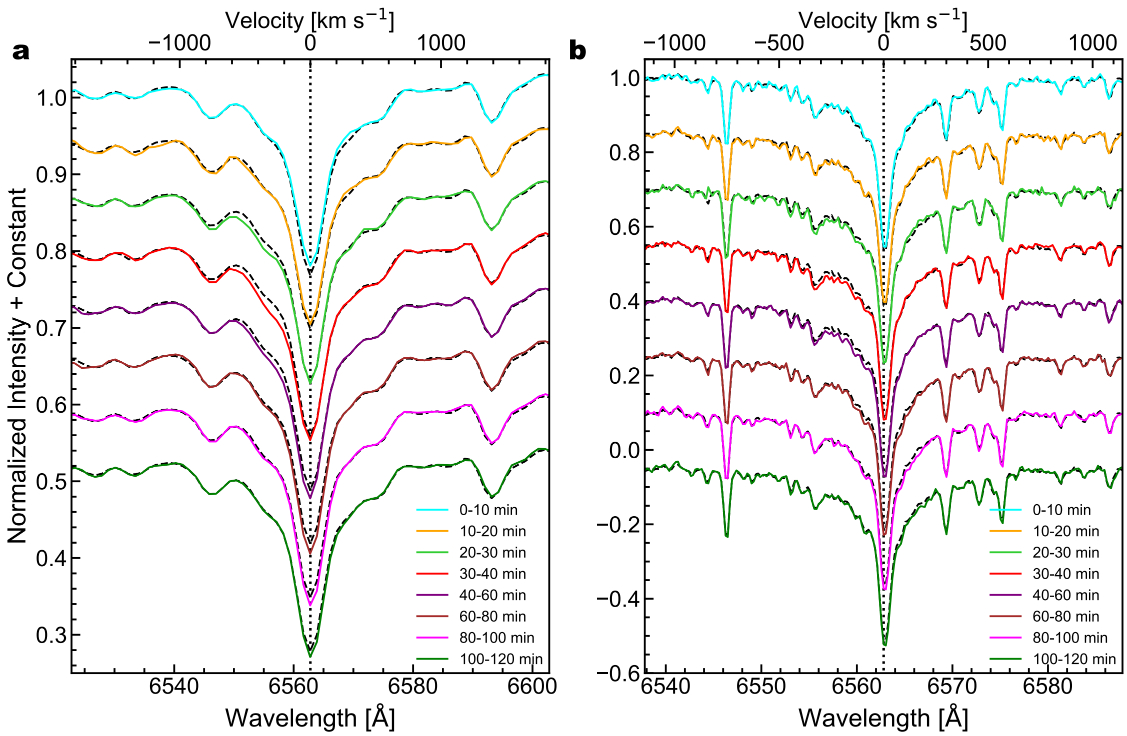


**Supplementary Fig. 3: Observed H$\alpha$ spectra during a superflare on EK Dra.** **(a)** H$\alpha$ spectra observed with Seimei Telescope/KOOLS-IFU (wavelength resolution $\lambda/\Delta\lambda \sim$ 2,000). Each colored spectrum indicates the averaged spectrum for each time indicated in the legend, and the background black dashed lines are the pre-flare template spectra. The spectra are normalized by the continuum level and the constant values are added to the spectra for visibility. The indicated times in the legend correspond to the times indicated in the horizontal axis of Fig. 1**(a-d)**. The dotted vertical line indicates the line center wavelength (6562.8 Å). **(b)** H$\alpha$ spectra observed with Nayuta Telescope/MALLS (wavelength resolution $\lambda/\Delta\lambda \sim$ 10,000). The plots are almost the same as panel **(a)**. Note that the range of the horizontal axis is different from panel **(a)** for visibility.

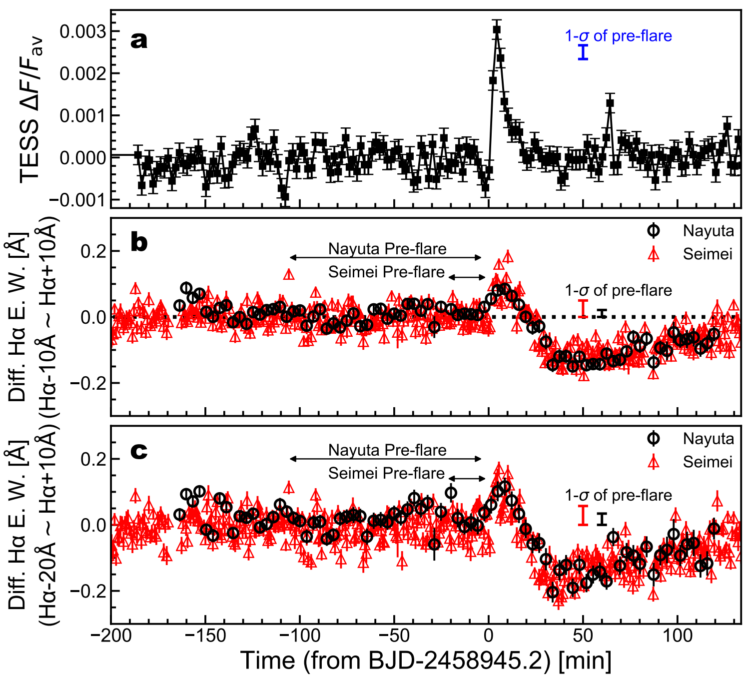


**Supplementary Fig. 4: Light curve of a superflare on EK Dra with a longer period than Fig. 1. (a)** TESS white-light light curve. The blue point indicates the 1-$\sigma$ value (0.00033) of the pre-flare brightness variation during -150 min – 0 min. **(b)** Light curves of the H$\alpha$ E.W.. The H$\alpha$ emissions were integrated within $\pm$10 Å from the H$\alpha$ line center (6562.8 Å. The black and red error bars indicate the 1-$\sigma$ value (0.050 and 0.021) of the pre-flare light curves observed by Nayuta Telescope/MALLS and Seimei Telescope/KOOLS-IFU, respectively. These error values are measured for -150 min – 0 min. The periods to make the pre-flare reference spectra are also indicated with black arrows in the panel (i.e., 30 data points before the flare onset). **(c)** The panel is essentially the same as panel **(b)**, but the H$\alpha$ emissions were integrated between 6562.8 - 20 Å and 6562.8 + 10 Å.

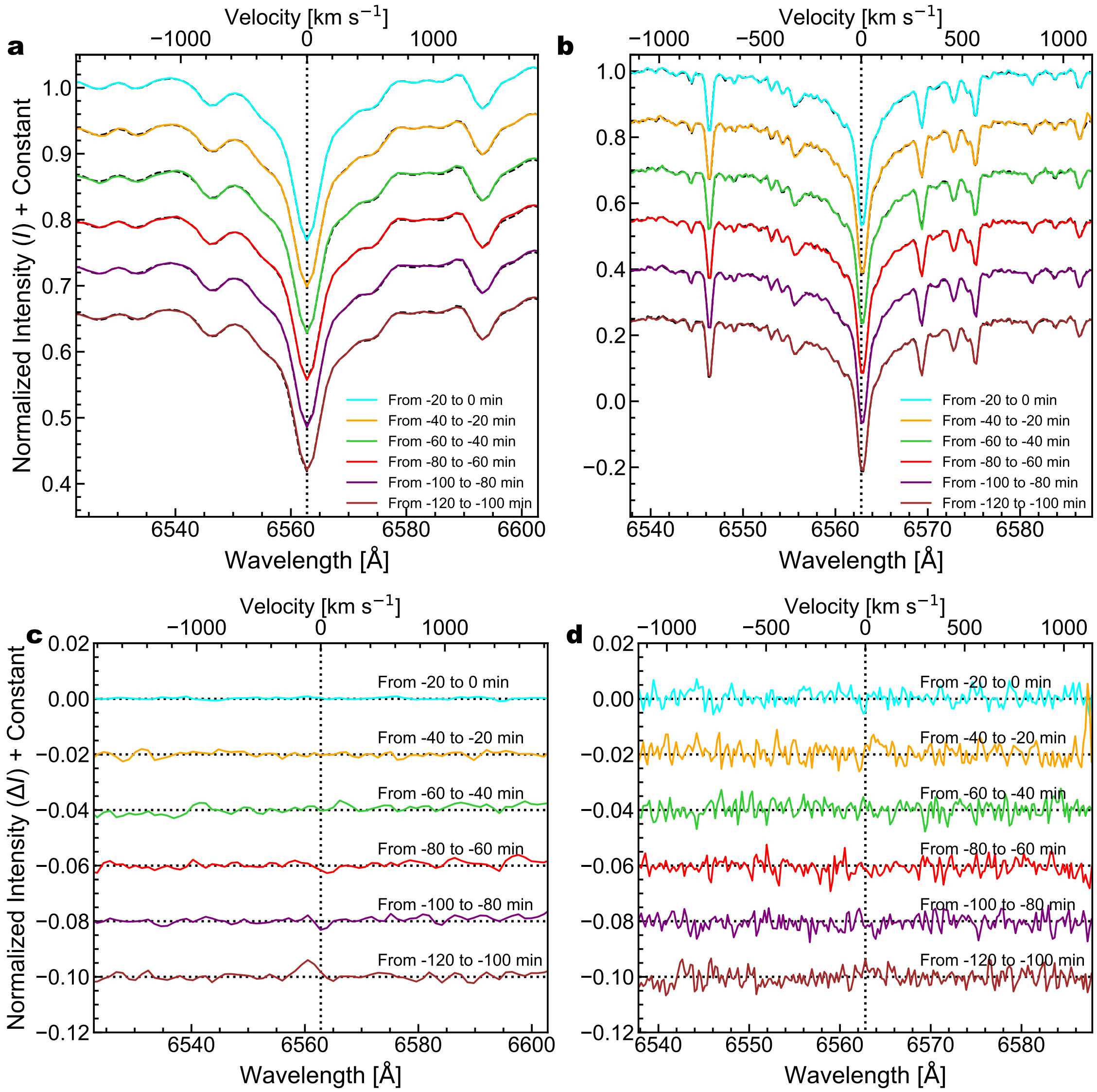


**Supplementary Fig. 5: Time-resolved pre-flare H$\alpha$ spectra observed by Seimei Telescope/KOOLS-IFU (a, c) and Nayuta Telescope/MALLS (b, d). (a, b)** colored lines indicate pre-flare H$\alpha$ spectra from -120 min to 0 min before the flare starts. Each colored spectrum indicates the averaged spectrum for the periods in the legend. The background black dashed lines are the pre-flare template spectra averaged for all 30 data points before the flare onset (the same ones in the Fig. S3). The frame 1-30 correspond to the observational period indicated with black arrows in Fig. S4 **(b,c)**. The vertical dotted vertical line indicates the line center wavelength (6562.8 Å). **(c, d)** The residual of the pre-flare H$\alpha$ spectra (colored lines in panel **(a, b)**) subtracted by the 30-frames-averaged spectra (black lines in **(a, b)**).

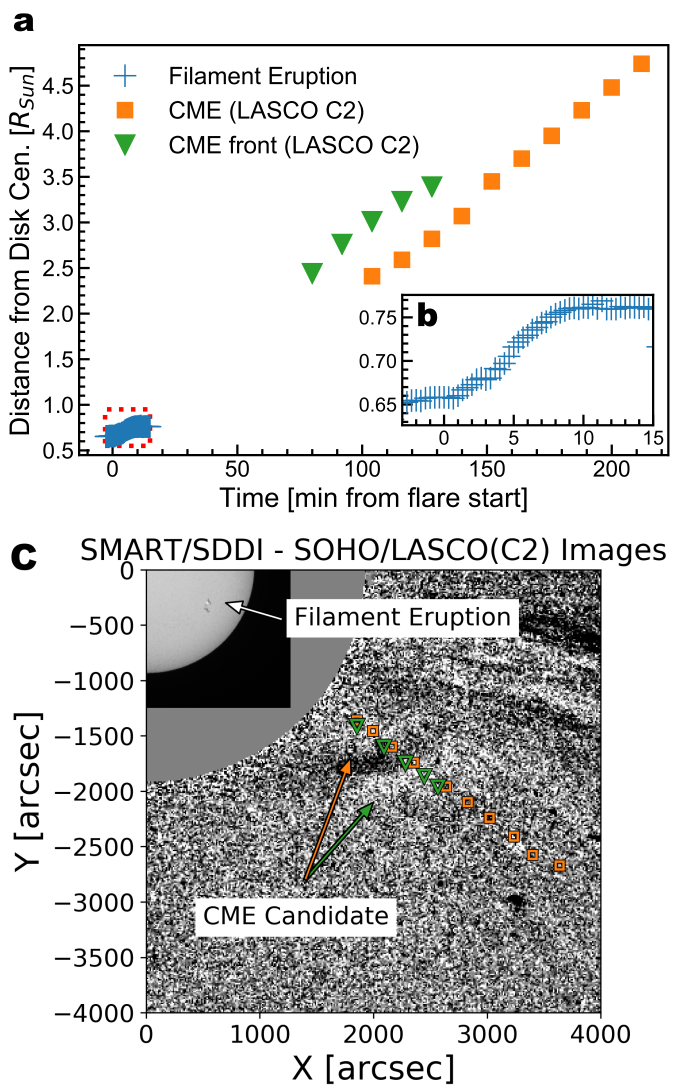


**Supplementary Fig. 6: A CME candidate associated the flare and filament eruption on 7 July, 2016, observed by SOHO/LASCO (C2).** **(a)** Temporal evolution of height of filament eruptions and corresponding CMEs. There are two components for this CME candidate (green and oranges for the leading and following materials). **(b)** The expanded figure of the temporal evolution of filament eruption in panel **(a)**. **(c)** The running difference image of coronagraph observed by SOHO/LASCO (C2) at 09:48:05.9 UT. The leading and following CME candidates are indicated with green and orange colors, respectively. The H$\alpha$ image of filament eruption observed by SMART/SDDI is also plotted as a reference, but the time is different from the SOHO/LASCO image. Furthermore, the horizontal and vertical axis corresponds to the distance from the solar disk center in the unit of arcsec. The SOHO/LASCO movie is available online (see section "Solar data analysis (continued from Methods)").

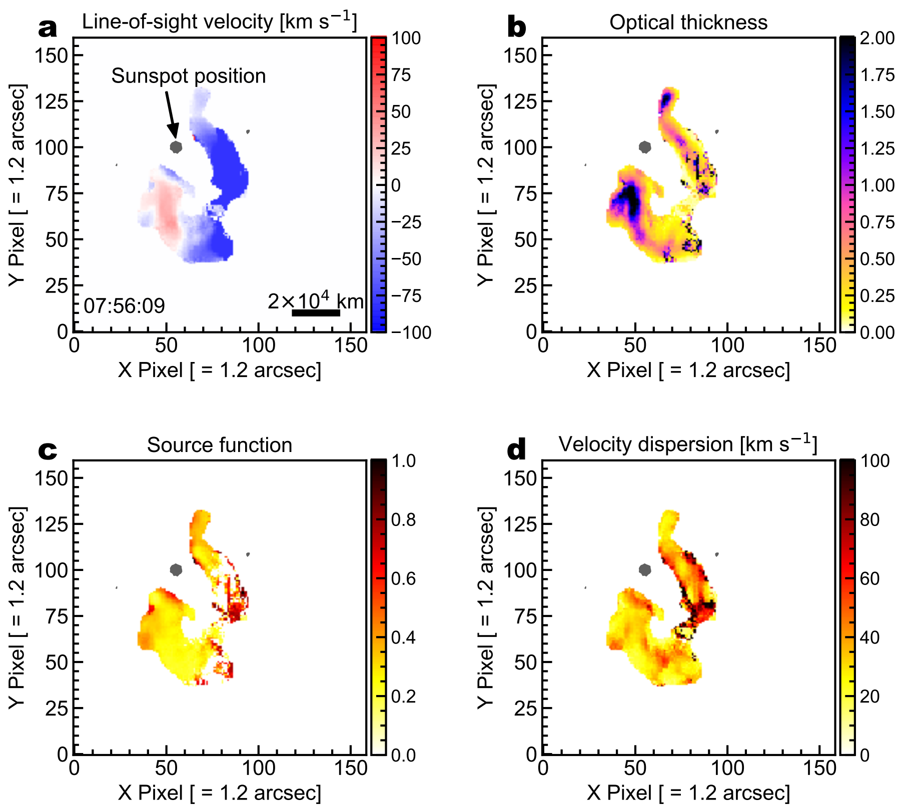


**Supplementary Fig. 7: Spatial distribution of parameters of the solar filament eruption.** The spatial distribution of line-of-sight velocity, optical depth, source function, and velocity dispersion for the solar filament eruption in Fig. 2 and Extended Data Fig. 4 is plotted in panel **(a)**, **(b)**, **(c)**, and **(d)**, respectively. Only the cool-plasma regions having enough large area are shown here. Also, gray regions are the simplified sunspot locations. The horizontal and vertical axes represent the x-y plane on the solar disk where one pixel corresponds to 1.2 arcsec.

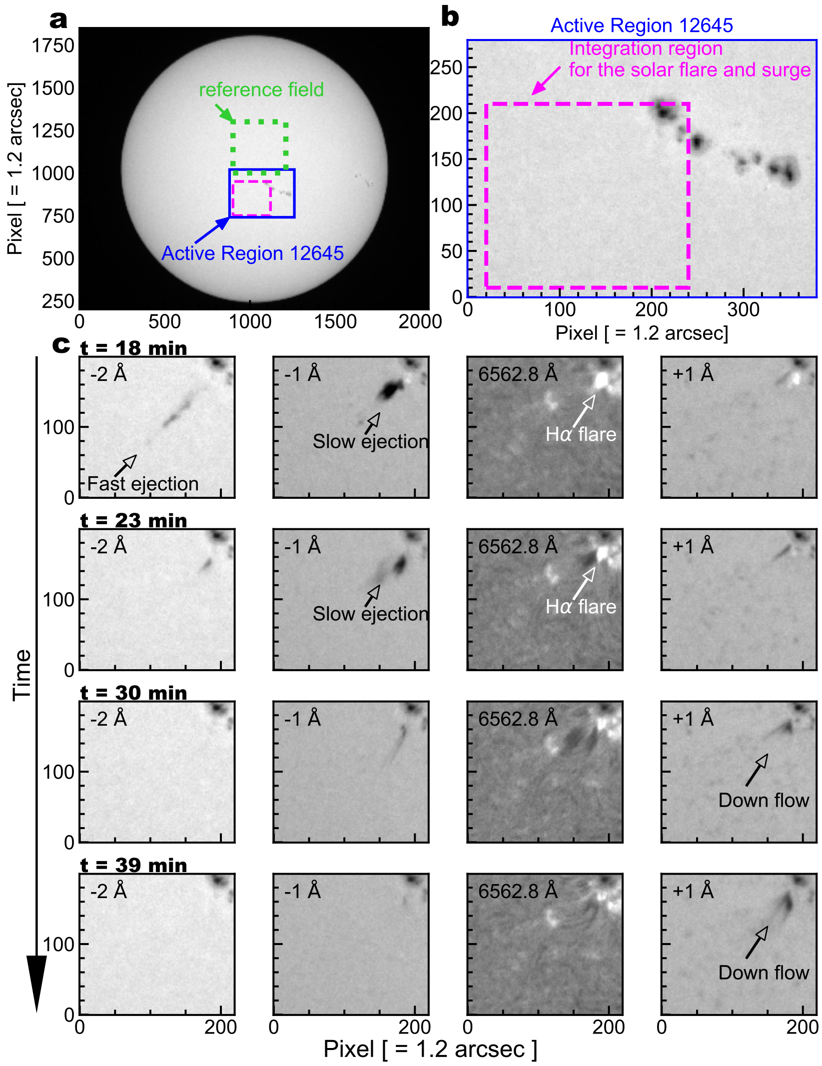


**Supplementary Fig. 8: A solar flare on 2 April, 2017, observed by SMART telescope/SDDI at Hida observatory. (a)** Full disk image of the Sun at the H$\alpha$ line wing (6559.8 Å). The horizontal and vertical axis denote the image pixels whose size is about 1.2 arcsec in the x-y plane. The green region is a quiet region used as a reference to make the H$\alpha$ spectra. **(b)** the blue region is the enlarged panel of the active region 12645. The magenta region is the region where the solar flare and surge could be seen. **(c)** The temporal evolution of solar images in the magenta region at the wavelength of 6560.8 ($-91$ km s$^{-1}$), 6561.8 ($-46$ km s$^{-1}$), 6562.8 (0 km s$^{-1}$), 6563.8 Å (+42 km s$^{-1}$). Emission and absorption features are indicated with white and black, respectively. The movie is available in Supplementary Video2.

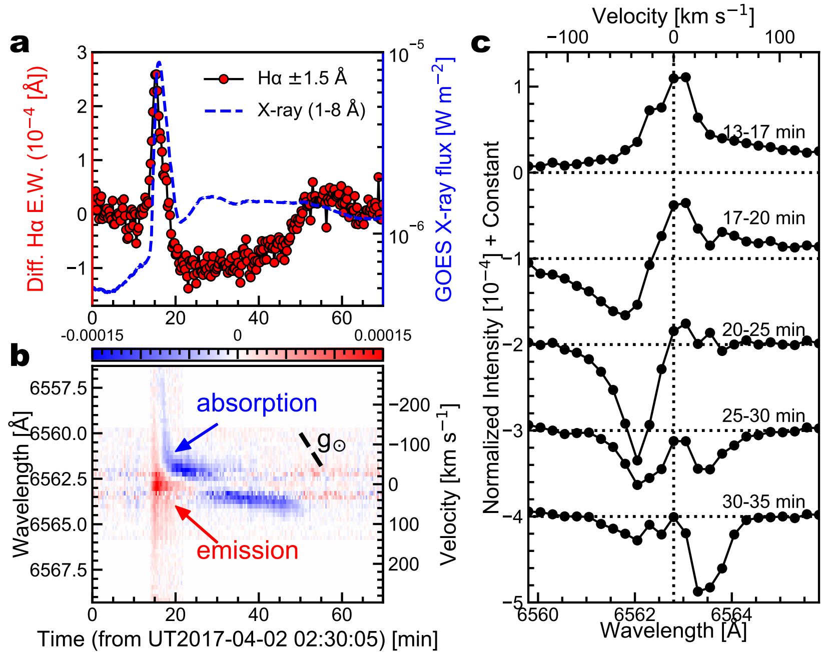


**Supplementary Fig. 9: The space-integrated light curves (a) and spectra (b-c) of a C8.0-class solar flare and surge on 2 April, 2017, observed with the SMART telescope. (a)** GOES soft X-ray (1-8 Å) and H$\alpha$ E.W. light curves of the solar flare are plotted as a blue dashed line and red circles, respectively. The H$\alpha$ emissions were integrated within $\pm$1.5 Å from the H$\alpha$ line center (6562.8 Å) and were divided by the full-disk continuum level, and the pre-flare level is subtracted. Time 0 is 14 minutes before the flare begins. **(b)** Two-dimensional pre-flare-subtracted H$\alpha$ spectra. The red and blue colors correspond to emission and absorption compared to the pre-flare levels, respectively. The dashed line indicates surface gravity at the solar surface. For the period from 02:43:50 to 02:51:44, all 73 wavelengths were available, while for the other periods, only 25 images from the H$\alpha$ line center $-$3.0 Å to the H$\alpha$ line center +3.0 Å are available in the archival database (the white regions in the four corners). **(c)** Temporal evolution of the pre-flare-subtracted H$\alpha$ spectrum shifted vertically by constant values for clarity. The H$\alpha$ spectra were produced by integrating the data over a large enough region to cover the flaring area. The intensities are normalized by the total solar continuum level. The vertical dotted line indicates the H$\alpha$ line center, and the horizontal dotted lines indicate the zero levels for each spectrum.

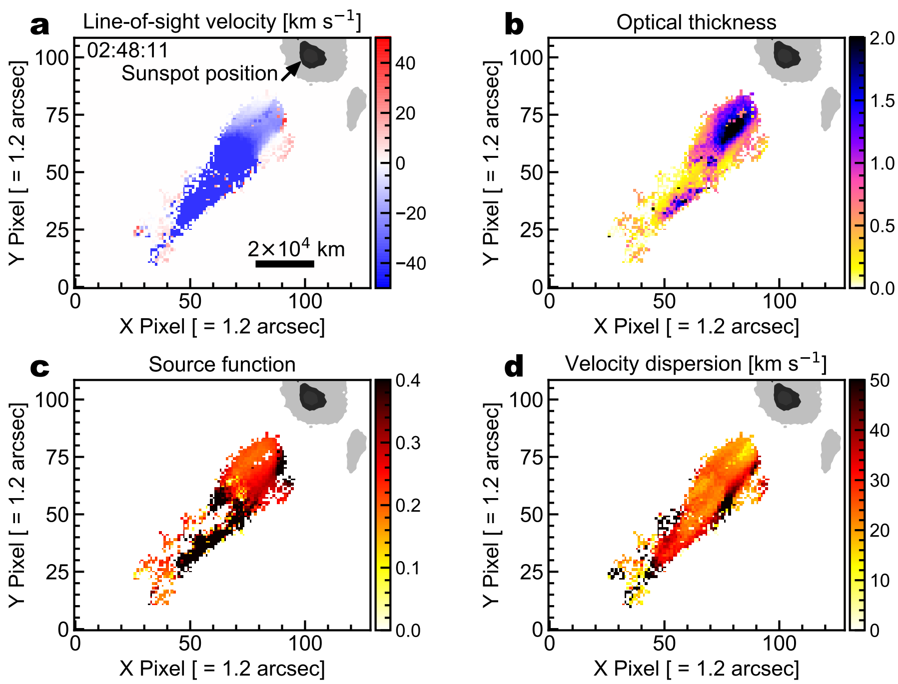


**Supplementary Fig. 10: Spatial distribution of parameters of the solar surge.** The spatial distribution of line-of-sight velocity, optical depth, source function, and velocity dispersion for the solar surge in Fig. S8 and Fig. S9 is plotted in panel **(a)**, **(b)**, **(c)**, and **(d)**, respectively. Only the cool-plasma regions having enough large area are shown here. Also, black and gray regions are the simplified spot umbra and penumbra, respectively. The horizontal and vertical axes represent the x-y plane on the solar disk where one pixel corresponds to 1.2 arcsec.